Supplemental Material: Enhancing Spin Coherence in Optically Addressable Molecular Qubits through Host-Matrix Control

S. L. Bayliss[†],[1,2] P. Deb[†],[1,3] D. W. Laorenza[†],[4,5] M. Onizhuk,[1,6]
G. Galli,[1,6,7] D. E. Freedman*,[4] and D. D. Awschalom*[1,3,7]

[1]*Pritzker School of Molecular Engineering, University of Chicago, Chicago, IL 60637, USA*
[2]*James Watt School of Engineering, University of Glasgow, Glasgow G12 8QQ, United Kingdom*
[3]*Department of Physics, University of Chicago, Chicago, IL 60637, USA*
[4]*Department of Chemistry, Massachusetts Institute of Technology, Cambridge, Massachusetts 02139, USA*
[5]*Department of Chemistry, Northwestern University, Evanston, IL 60208, USA*
[6]*Department of Chemistry, University of Chicago, Chicago, IL 60637, USA*
[7]*Center for Molecular Engineering and Materials Science Division, Argonne National Laboratory, Lemont, IL 60439, USA*

[†]These authors contributed equally to this work
*awsch@uchicago.edu, danna@mit.edu

I. SYNTHESIS

Glassware was either oven-dried at 150°C for at least four hours or flame-dried prior to use. Toluene, tetrahydrofuran (THF), diethylether (Et_2O), and hexanes were dried using a commercial solvent purification system from Pure Process Technology and stored over 4 Å sieves prior to use. All solvents were subjected to a test with a standard purple solution of sodium benzophenone ketyl in THF to confirm low $O_2$and H_2O content prior to use. 2-Bromo-5-fluorotoluene and magnesium (Mg) ribbon were purchased from Sigma Aldrich and used as received. Tin tetrachloride was purchased from Alfa Aesar and used as received. **1-Cr** (Cr(o-tolyl)$_4$), **2-Cr** (Cr(2,3-dimethylphenyl)$_4$), **3-Cr** (Cr(2,4-dimethylphenyl)$_4$), **1-Sn** (Sn(o-tolyl)$_4$), and Sn(2,3-dimethylphenyl)$_4$, and Sn(2,4-dimethylphenyl)$_4$, were synthesized under a N_2 atmosphere with either an MBraun Unilab Pro glovebox, Vacuum Atmosphere Nexus II glovebox, or

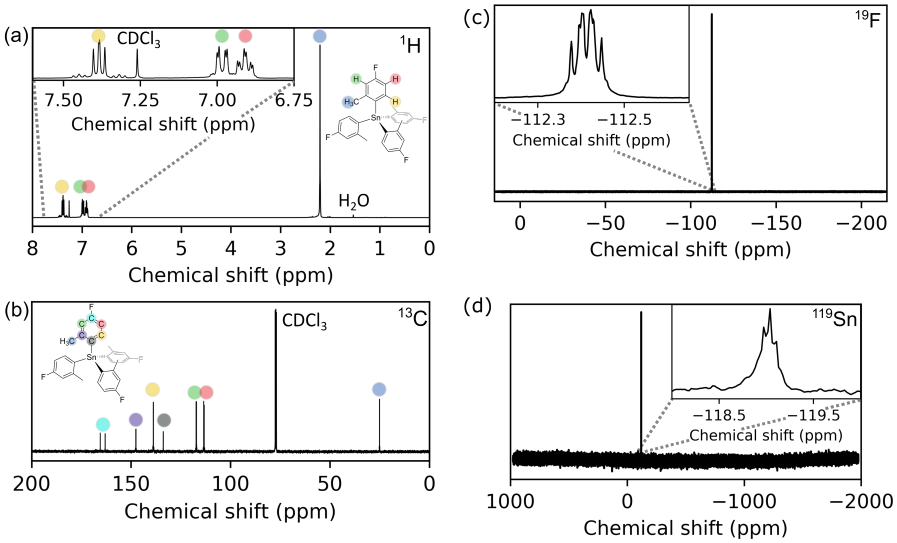

FIG. S1. (a) 400 MHz ^{1}H NMR spectrum of **2** in $CDCl_3$ at room temperature. ChemDraw molecular structure indicates the peak assignment given by the color of the highlighted H atom and the corresponding peak. The inset highlights the peak splitting of the aromatic ^{1}H nuclei. (b) 101 MHz ^{13}C NMR spectrum of **2** in $CDCl_3$ at room temperature. ChemDraw molecular structure indicates the peak assignment given by the color of the highlighted C atom and the corresponding peak. The individual peaks show splitting that corresponds to J coupling of the ^{13}C nuclei with the ^{19}F nucleus, with the largest J-coupling value of 248.0 Hz corresponding to the carbon atom directly bound to the fluorine atom. (c) 376 MHz ^{19}F NMR spectrum of **2** in $CDCl_3$ at room temperature. The inset shows the splitting of the central peak, likely a result of coupling to surrounding ^{1}H nuclei. (d) 149 MHz ^{119}Sn NMR spectrum of **2** in $CDCl_3$ at room temperature, with the inset showing the unresolved splitting of the single peak.

Schlenk techniques according to previously published literature methods [1–3]. 4-fluoro-2-methylphenylmagnesium bromide was prepared with slight modifications to literature procedure (see below). Once synthesized, all tin compounds are air stable and as such, may be worked up and handled outside of an inert atmosphere. Similarly, cocrystallized Cr:Sn single crystals and microcrystalline samples are stable over the course of several days after ambient exposure before noticeable loss of visible absorption intensity.

Synthesis of tetrakis(4-fluoro-2-methylphenyl)stannane (**2-Sn**): Mg ribbon (2.6 g, 106 mmol, 4 equiv.) was cut into ∼3-4 mm long pieces into a dry 250 mL three-neck round bottom flask under positive pressure of N_2. [Synthetic note: the freshly cut Mg ribbon typically resulted in faster initiation in the formation of the Grignard reagents than magnesium turnings.] The Mg ribbon was then 'knocked' (i.e., stirred) with a magnetic stir bar at the maximum rate of the stir plate for 16 hours under vacuum to further activate the Mg ribbon. The flask was then returned to a positive pressure of N_2 and 100 mL of Et_2O was added via cannula. The three neck round bottom flask was fitted with a reflux condenser and an addition funnel. Approximately 5-10% of a solution of 2-Bromo-5-fluorotoluene (5 g, 26.5 mmol, 1 equiv.) in 25 mL of Et_2O was added dropwise through the addition funnel to the stirring mixture of Mg and Et_2O. Upon initiation of the reaction when the solvent began to visibly boil, the remainder of the solution in the addition funnel was added dropwise over ∼10 minutes with continuous stirring to the reaction flask. The reaction was then heated under reflux conditions for 2 hours. The reaction flask was then cooled down to room temperature and filtered through a fritted Schlenk funnel to remove excess Mg. The resulting solution was then cooled to 0°C, at which point $SnCl_4$ (1.12 g, 4.33 mmol, 1/6 equiv.) was added dropwise to the solution via a syringe. A white solid precipitated immediately upon addition, likely an insoluble $SnCl_4$ -Et_2O adduct. The reaction flask was then brought back to reflux conditions for 18 hours, over which time the white solid was solubilized in the reaction mixture. The reaction mixture was cooled to room temperature and 2-3 mL of a 1% hydrochloric acid (HCl) aqueous solution was added dropwise to the reaction mixture to quench excess 4-fluoro-2-methylphenylmagnesium bromide. (Note: This step can result in substantial heating if a large amount of 4-fluoro-2-methylphenylmagnesium bromide remains. Do not add the HCl solution rapidly to the reaction flask.) Once no heating occurred upon dropwise addition of the HCl solution to the reaction mixture, 100 mL of the 1% HCl solution was added to the reaction flask slowly. The mixture was transferred to a separatory funnel. The aqueous layer was washed with 3x75 mL of Et_2O. The combined organic washes were then dried with magnesium sulfate and the solvent was removed with rotary evaporation. The crude product was isolated as either a yellowish oil or a yellow solid. The resulting oil was extracted into toluene (∼10 mL) and filtered through a pad of celite to remove any insoluble solids. The toluene solution was then layered under 10 mL of hexanes in a 20 mL scintillation vial. The vial was stored at −35°C for one week, at which point colorless crystals suitable for X-ray diffraction were collected. Typical reaction yields based on resulting crystalline product were 0.75-1.0 g (1.35 mmol-1.8 mmol, 31-42% yield based on the Sn pre-cursor). Crystalline product could also be obtained via THF/hexanes or DCM/hexanes layering at −35°C or slow diffusion of hexanes into toluene, THF, or DCM. ^{1}H NMR (400 MHz, $CDCl_3$, 298 K) δ 7.48 – 7.28 (tt, J=26.1, 7.6) 1H), 6.98 (dd, J=10.5, 2.6 Hz, 1H), 6.91 (td, J=8.5, 2.7 Hz, 1H), 2.20 (s, 3H). ^{13}C NMR (101 MHz, $CDCl_3$, 298 K) δ 164.26 (d, J=248.0 Hz), 147.54 (d, J=7.0 Hz), 138.77 (d, J=7.6 Hz), 133.80 (d, J=3.6 Hz), 117.17 (d, J=19.6 Hz), 113.33 (d, J=19.4 Hz), 25.20 – 24.82 (m). ^{19}F NMR (376 MHz, $CDCl_3$, 298 K) δ -112.41 (ddt, J=14.3, 11.1, 4.9 Hz) ^{119}Sn NMR (149 MHz, $CDCl_3$, 298 K) δ -119.04 (m, J=10.0 Hz). See Fig. S1.

II. CRYSTALLIZATION AND X-RAY STRUCTURE DETERMINATION

All crystallizations were carried out under a N_2 atmosphere in a Vacuum Atmosphere Nexus II glovebox. Diluted crystals of **1**, **3**, and **4** were prepared as described previously [3]. In an analogous manner to these crystallization methods, 200 mg of **2-Sn** and 2 mg of **1-Cr** were dissolved in 3 mL of THF. This solution was filtered through Celite and then layered under 6 mL of Et_2O. The crystallization was left at −35°C for four weeks, during which time transparent, pink crystals began to grow. The crystals were left to grow for another four weeks, at which point, several millimeter sized crystals had formed. One of these crystals were cleaved with a razor blade to obtain a sufficiently thin (∼100-200 micron thick) crystal. The thin crystal was essential to obtain sufficiently strong microwave field at the probed subensemble to drive the spin transitions in the pulsed optically detected magnetic resonance (ODMR) experiments. Note, the diluted crystals are relatively stable in ambient atmosphere with no noticeable degradation over the course of ∼10 days. Manipulations with the crystals may, therefore, occur outside of a glovebox. To minimize the possibility of sample degradation, samples measured herein were handled and mounted on the coplanar waveguide (see Experimental Methods) under a N_2 atmosphere inside of a glovebox.

Single crystal X-ray diffraction data were collected in the X-ray crystallography lab of the Integrated Molecular Structure Education and Research Center (IMSERC) at Northwestern University. Single crystals of **2-Sn** suitable for X-ray diffraction analysis were coated in Paratone N oil and mounted on a MiTeGen MicroLoopTM. Single crystal data were collected on a Rigaku XtaLAB Synergy (Single source) with a micro-focus sealed X-ray tube PhotonJet (MoKa)

Table I. Crystallographic data for the structure refinement of **2-Sn** measured at 100 K.

	Sn(4-fluoro-2methylphenyl)$_4$(**2-Sn**)
Empirical formula	$C_{28}H_{24}F_4$ Sn
Formula weight	555.18 g/mol
Temperature	99.98(14)
Radiation	MoKα ($\lambda = 0.71073$ Å)
Crystal system	Orthorhombic
Space group	Pbcn
Unit cell dimensions	$a = 16.5918(2)$Å, $\alpha = 90°$ $b = 17.1973(2)$Å, $\beta = 90°$ $c = 17.0037(3)$Å, $\gamma = 90°$
Volume	4851.74(12) Å^3
Z	8
Density (calculated)	1.520 g/cm^3
Absorption coefficient	1.097 mm^{-1}
F_{000}	2224
Crystal color	Colorless
Crystal size	0.64 x 0.36 x 0.28 mm^3
2θ range	2.3720 to 38.3420°
Index ranges	$-28 \leq h \leq 26$ $-28 \leq k \leq 27$ $-21 \leq l \leq 28$
Reflections collected	68023
Independent reflections	12583 [$R_{int} = 0.0363$]
Absorption correction	Gaussian
Data / restraints / parameters	12583 / 0 / 302
Goodness-of-fit on F$^{2(a)}$	1.024
Final R indices [I $> 2\sigma$(I)]$^{(b)}$	$R_1 = 2.77\%$, $wR_2 = 6.38\%$
R indices (all data)	$R_1 = 3.75\%$, $wR_2 = 6.77\%$
Largest diff. peak and hole	0.551 and -1.110 e.Å^{-3}

$^{(a)}$GooF= $[\sum[w(F_o^2 - F_c^2)^2/(n-p)]^{1/2}$where n is the number of reflections and p is the total number of parameters refined.
$^{(b)}R_1 = \sum ||F_o| - |F_c|/\sum |F_o|; wR_2 = [\sum[w(F_o^2 - F_c^2)^2]/\sum[w(F_o^2)^2]]^{1/2}$

radiation source, HyPix CCD detector and an Oxford Cryostream cooler. Raw data were integrated using CrysAlisPro. Absorption corrections were applied using multi-scan absorption correction with the SCALE3 ABSPACK module in CrysAlisPro [4]. The space groups of each compound were determined by examination of systematic absences, E-statistics, and successive refinement of the structure. Using the OLEX2 interface [5], the structures were solved with intrinsic phasing (SHELXT) [6] methods and further refined using least squares minimization with SHELXL [7]. Thermal parameters for all non-hydrogen atoms were refined anisotropically. All hydrogen atoms were fixed at ideal positions, refined using a riding model for all structures, and refined using isotropic displacement parameters derived from their parent atoms. Crystallographic details for **2-Sn** are listed in Table I.

III. EXPERIMENTAL METHODS

We use a cryogenic confocal microscopy setup to optically excite the molecular color centers and collect their photoluminescence. The molecular crystal sample is mounted on a coplanar waveguide for microwave delivery, which in turn is mounted inside a closed cycle cryostat (Montana Instruments, Cryostation s100) on an XYZ piezo stage (Attocube: 2×ANPx101/RES/LT, 1×ANPz102/RES/LT), to allow translation of the sample. To measure the photoluminescence spectrum in Fig. 1(d) we use a 785 nm laser diode (Thorlabs, FPL785S-250). For all other experiments we use resonant excitation at the zero-phonon line. We resonantly excite using a narrow linewidth tunable laser (Toptica, DL pro) and shortpass the excitation beam to remove spurious wavelengths. To monitor the resonant excitation wavelength and mode behavior, we use fiber beam splitters to direct parts of the beam into a wavemeter (Bristol, 621A) and a scanning Fabry-Perot interferometer, respectively (Thorlabs, SA200-8B). We use an acousto-optic modulator (AOM, Gooch and Housego 15200-.93) driven by a radio frequency (RF) AOM driver (Gooch and Housego, R21200-1DS) to generate optical pulses. An arbitrary waveform generator (AWG, Tektronix, AWG5014C) sets the timing for control pulses to all experimental components, including this RF driver. A linear polarizer (Thorlabs, LPNIR100-MP2) in conjunction with a motorized half-wave plate (HWP, Thorlabs, AHWP10M-980 and PRM1Z8), is used to control the

Table II. Nuclear spin densities of tin host matrices

Host	η (N/nm^3)	$\eta_{^1H,^{19}F}\eta$ $(N_{^1H,^{19}F}/nm^3)$	$\eta_{adj}(N\cdot\mu_N/nm^3)$	$\eta_{adj,^1H,^{19}F}(N_{^1H,^{19}F}\cdot\mu_N/nm^3)$
1-Sn	51.68	50.85	142.10	142.02
2-Sn	46.94	46.17	128.28	127.86
3-Sn	55.13	54.36	151.94	151.83
4-Sn	44.53	43.91	126.13	126.04

optical polarization. The excitation beam passes through a broadband 50:50 beamsplitter (BS, Thorlabs, BSW29R), which separates the excitation and collection paths. A fast steering mirror (Newport, FSM-300) is used to scan the laser across the sample. The excitation beam is focused onto the sample using a microscope objective (Olympus, LCPLN100XIR, NA = 0.85), mounted inside the cryostat. The PL is collected by the same objective, reflects off the 50:50 BS, and the laser scatter is removed using a longpass filter. The PL is coupled either into a single-mode fiber to be detected with a superconducting nanowire single photon detector (SNSPD, Quantum Opus, Opus One), or into a multi-mode optical fiber. The multi-mode path is sent to a spectrometer (Acton, SpectraPro 2500i) combined with a CCD (Princeton Instruments, Pylon-IR), which is used for spectral measurements. Static magnetic fields were applied to the sample using a permanent magnet outside the cryostat. This magnet is mounted on a motorized linear translation stage (Zaber, X-LSQ150A), and the field at the sample is calibrated using a Gaussmeter. For the homogeneous linewidth extraction, the laser sidebands are generated using an electro-optic modulator to which we supply a microwave drive using a signal generator (Agilent, E8257D).

For the experiments involving gated readout [i.e., Figs. 2, 3, 4, 5(b)] the SNSPD output is amplified to a transistor-transistor logic level using a pulse converter (Pulse Research Lab, PRL-350TTL). These pulses are gated by switches (Minicircuits, ZASWA-2-50DRA+) that are controlled by the AWG, and collected using counters in a data acquisition card (DAQ6363, National Instruments). For the hole-burning experiment [Fig. 5 (a)], the counts from the SNSPD are sent to a time tagger (Swabian Instruments, Time Tagger 20), which is triggered by the AWG. Microwave signals are generated by a signal generator (SG396, Stanford Research Systems or Agilent, E8257D). For pulsed ODMR experiments, microwave pulses were amplified using a high-gain, broadband amplifier (25S1G4A, Amplifier Research). For Fig. 2(c) in the main text we define the PL contrast as [PL(on)-PL(off)]/[PL(on)+PL(off)] where PL(on) and PL(off) are the PL on and off resonance respectively. This definition ensures a maximum contrast of 100%. For the Hahn echo experiments, we phase-cycle the final microwave pulse, and take the difference in PL from the two phases.

IV. FURTHER EXPERIMENTAL DATA AND DISCUSSION

Nuclear spin density in different host matrices. The nuclear spin densities, η, were determined from the crystal structures of **1-Sn**, **2-Sn**, **3-Sn**, and **4-Sn** using the formula: $\eta = \frac{\sum N_i}{V}$, where N_i is the number of each nuclear spin-bearing isotope (^{1}H, ^{13}C, ^{19}F, ^{115}Sn, ^{117}Sn, and ^{119}Sn) in the unit cell, $\sum N_i = N$, and V is the unit cell volume in nm^3. As each nuclear spin-bearing isotope exhibits a unique magnetic moment, we also normalized η as follows: $\eta_{adj} = \frac{\sum N_i\cdot\mu_i}{V}$, where μ_i is the nuclear magnetic moment of the nuclear spin bearing isotope in μ_N. In Table II, we observe 10-20% changes in both η and η_{adj} between each host. Additionally, **1-Sn**, **2-Sn**, **3-Sn**, and **4-Sn** exhibit similar molecular concentrations of 2.74, 2.96, 2.50, and 2.42 mol/L. The small variations in η and molarity across host matrices illustrates that the 250-500% enhancement in T_2 arises primarily from an increase in E, as opposed to changes in the nuclear spin composition or molecular concentration of the host. Finally, to determine the dominant source of magnetic noise in the environment, we calculated $\eta_{^1H,^{19}F}$ and $\eta_{adj,^1H,^{19}F}$ where we calculate η, as outlined above, but exclude ^{13}C, ^{115}Sn, ^{117}Sn, and ^{119}Sn. In general, $\eta \approx \eta_{^1H,^{19}F}$ for each host. These results illustrate that ^{1}H and ^{19}F spins are the most substantial source of environmental noise.

Chromium sites in 2. We investigated the multiple possible chromium insertion sites in **2** through optically detected magnetic resonance (ODMR). Fig. S2(a) shows continuous-wave (cw) ODMR spectra under different magnetic field configurations. Here B_x, B_y, B_z refer to orthogonal orientations in the lab frame. For a single site, we would expect a maximum of three transitions in total (i.e., $|0\rangle \leftrightarrow |-\rangle$, $|0\rangle \leftrightarrow |+\rangle$ $|-\rangle \leftrightarrow |+\rangle$). The fact that we resolve more than three transitions indicates that there is more than one magnetically inequivalent Cr incorporation site. We find the main features of the experimental heat maps can be simulated using two sites which differ in their orientation by approximately a 45° rotation. Fig. 2(a) in the main text is the B_z orientation of Fig. S2(a) and uses the same simulation parameters i.e., $D = 5.55$ GHz, $E = 1.85$ GHz, and a g-factor of 2.05 (possibly representing a slight field mis-calibration) using the Euler angles for the green site in Fig. S2(a). To further resolve the Cr sites, we performed ODMR at a higher magnetic field [~ 70 mT, Fig. S2(b)]. We observed more than four transitions in the lower-frequency part of the spectrum indicating at least three magnetically distinct Cr-site orientations. Examining

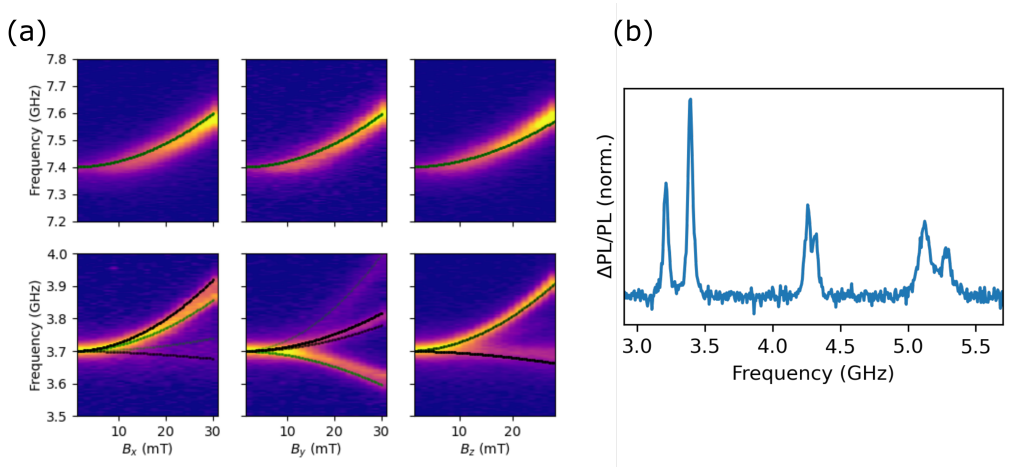

FIG. S2. Cr sites in **2**. (a) ODMR as a function of magnetic field and frequency for different field orientations. The points are simulations for two different sites (green and black respectively). The transparency of the points is given by the simulated ESR matrix element for the transition, such that both the frequencies and the oscillator strengths of the transitions can be taken into account for comparison with the experimental data. Each site is given a global orientation used for all the simulated traces. (b) ODMR at higher magnetic field ($B_y \sim 70\,\mathrm{mT}$) showing six transitions in the lower-frequency branch, indicating at least three magnetically inequivalent Cr sites.

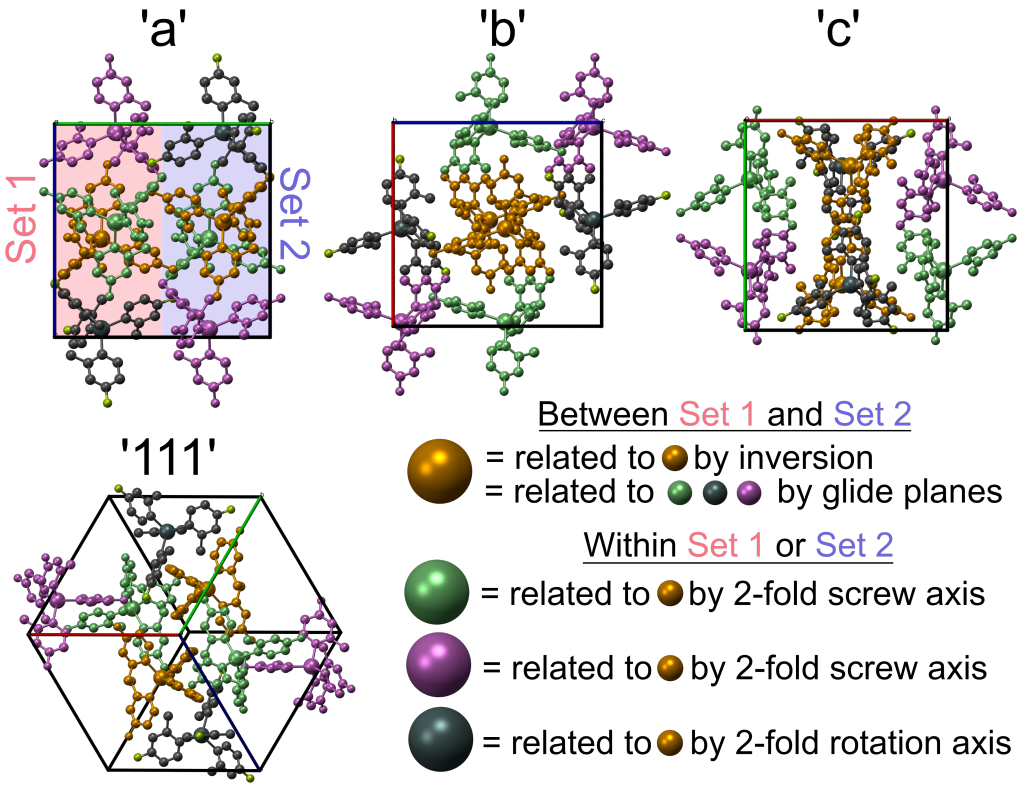

FIG. S3. Crystallographic projections of the filled unit cell of **2-Sn** with 8 total molecules (Z=8) viewed along the a, b, c, and [111] directions. To illustrate the crystallographic symmetry relationships between sites, we identify two sets of molecules among these eight, noted as Set 1 and Set 2. The two central, orange molecules are related by inversion symmetry. The orange molecules are related to the remaining three molecules in each set by the symmetry elements noted in the legend.

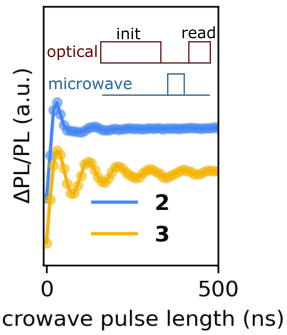

FIG. S4. Zero-field Rabi oscillations for **2** and **3**

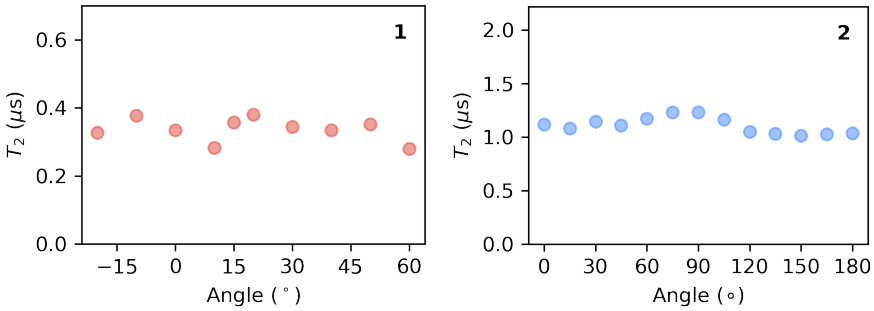

FIG. S5. Experimental T_2 times for **1** and **2** as a function of magnetic field orientation. For **1**, $B \sim 3\,\mathrm{mT}$ and 0° is approximately aligned with the quantization axis of the zero-field splitting tensor, which is the long-axis of the crystal. For **2**, $B \sim 5\,\mathrm{mT}$ and since the Cr-site orientation in the lab frame was not determined, the angle is defined in the lab frame.

the crystal structure of **2-Sn**, the unit cell has a Z´ = 1 and Z = 8. Thus, the asymmetric unit of the crystal is a complete single molecule while the unit cell is filled by eight, symmetry-related molecules with a local site symmetry of C_1 at each tin center. Assuming **1-Cr** substitutes directly into the tin sites in **2-Sn**, the structure allows for a maximum of eight unique orientations of the chromium site. The symmetry equivalence between sites (see Fig. S3) suggests that the chemical environment, and consequently, the ground state spin structure of all sites, will be equivalent at zero magnetic field (*i.e., D, E* will be equal for all sites). Under non-zero applied field, the spin transitions for sites of differing orientation should exhibit unique field responses that may be more easily resolved at higher fields, as we observe. However, without knowing the orientation of the zero-field splitting tensor in the molecular frame or the precise orientation of **1-Cr** in the **2-Sn** host, we cannot say which of these sites will be magnetically inequivalent for the **1-Cr** center. While we cannot rule out the possibility of magnetic equivalence without understanding the exact Cr site symmetry within this host, the local symmetry of the tin molecule does not contain rotational axes that would enforce magnetic equivalence, such that the native **2-Sn** crystalline environment allows for multiple (maximum of eight) magnetically inequivalent sites.

Microwave-pulse calibration. π-pulse lengths were determined from Rabi oscillation measurements in which we measure the changes in PL as a function of a variable microwave pulse length, using the sequence outlined in Fig. S4. (For Rabi oscillations for **1**, see Ref. [3].) The zero-field data for **2** have contributions from multiple Cr-site orientations, as well as from the degenerate $|-\rangle \leftrightarrow |0\rangle$ and $|-\rangle \leftrightarrow |+\rangle$ transitions, giving rise to more frequency components than in **3**.

T_2 orientation dependence. Fig. S5 shows T_2 as a function of magnetic field orientation for **1** and **2**, highlighting the weak dependence on magnetic field alignment in our experiments. This weak dependence on field orientation is also observed theoretically (Fig. S15).

Hahn echo data. Fig. S6 shows the Hahn echo traces for for **1**, **2** and **3** for different magnet fields. To extract T_2 times, Hahn echo traces were fit to a stretched exponentional of the form $e^{-\left(\frac{2\tau}{T_2}\right)^{\alpha}}$ where α is the stretch factor, and 2τ the free-evolution time. Fig. S6 shows extracted T_2 times and stretch factors for different magnetic fields. To reproduce the functional form of the Hahn echo traces across the different magnetic fields, we use the stretch factor as a fit parameter. As highlighted in Fig. S7(a)/(b), we find that different stretch factors better reproduce the Hahn echo traces at different magnetic fields. We note that, as highlighted in Fig. S7(a)/(b), the choice of stretch factor

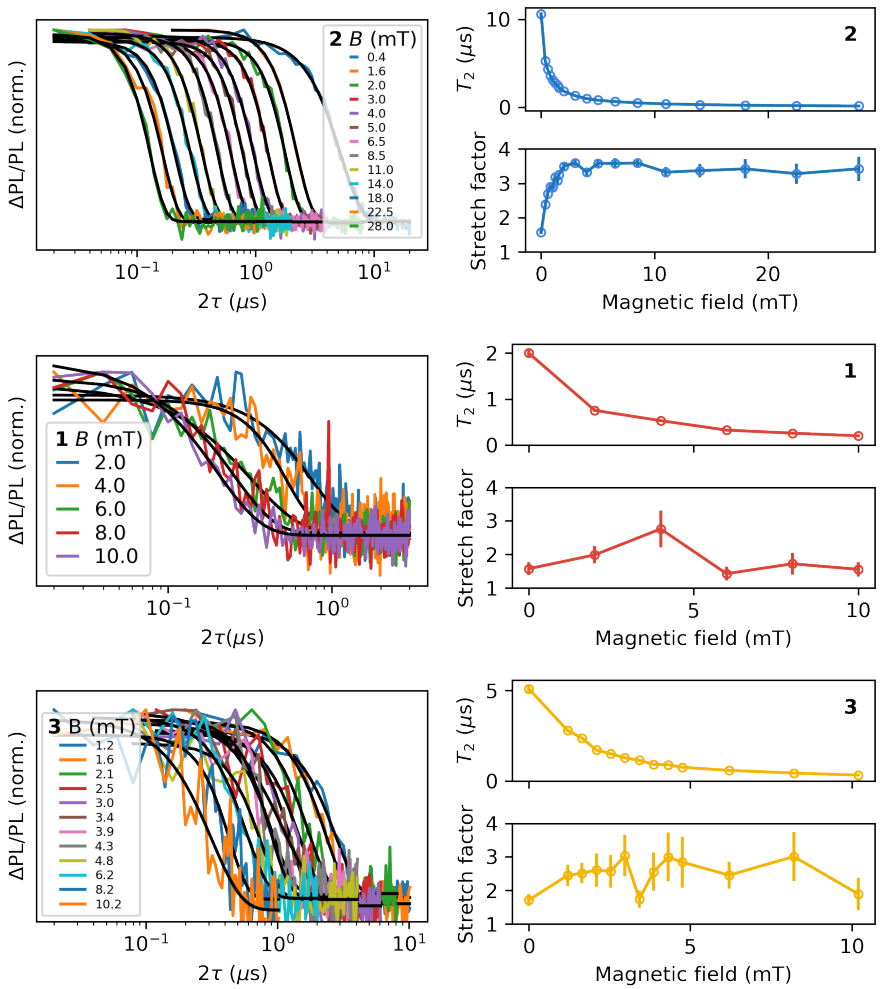

FIG. S6. Hahn-echo data for **1**, **2** and **3**.

does not significantly influence the extracted T_2 times. Fig. S7(c) shows the stretch factors calculated for **2** using gCCE calculations. These calculations show an increase in stretch factor as a function of magnetic field, which we also observe experimentally (Fig. S6), and highlight that the noise from the nuclear spin bath varies with the applied field. We note that while stretch factors have been used to infer information on the properties of the noise source in systems without clock transitions [8], in systems with clock transitions, the reduced noise sensitivity changes the effective noise spectrum, making the extraction of noise spectra from Hahn-echo data more challenging [9].

T_2 and df/dB. As noted in the main text (Section C, last paragraph), in addition to changing the noise *sensitivity* (i.e., df/dB where f is the ODMR frequency and B magnetic field), the increase in magnetic field also affects the nuclear spin bath dynamics, i.e., the noise *source*. This leads to a T_2 which decreases more rapidly with magnetic field than by considering df/dB alone (Fig. S8) since both the noise *and* the noise sensitivity are increasing. The increase in nuclear spin-bath noise with magnetic field arises due the changing relative importance of the (fixed) spin-spin interactions and the (variable) Zeeman interaction, as described for nitrogen vacancy centers in Ref. [10]. In molecular systems, the qualitative behavior of the dependence of T_2 on field due to this effect is similar, but the characteristic field scale is larger, as the hydrogen bath leads to stronger spin-spin interactions. The drop in T_2 with field for **1**, which does not have a clock transition, and therefore should have a constant df/dB, highlights the importance of considering the increase in noise with magnetic field, in addition to df/dB.

Zero-field Hahn-echo of 2. At zero field for **2**, in which $E = D/3$, the $|0\rangle \leftrightarrow |-\rangle$ and $|-\rangle \leftrightarrow |+\rangle$ transitions are degenerate, each occurring at $D - E = 2E = 3.7\,\text{GHz}$. In our cluster-correlation calculations we calculate the coherence times for each of these transitions separately [Fig. 3(d)], showing a similar T_2 for both transitions. The $|0\rangle \leftrightarrow |-\rangle$ transition requires microwaves polarized along the y-axis of the molecular frame, while the $|-\rangle \leftrightarrow |+\rangle$ transition requires microwaves polarised along the z-axis of the molecular frame. For microwaves polarised along y,

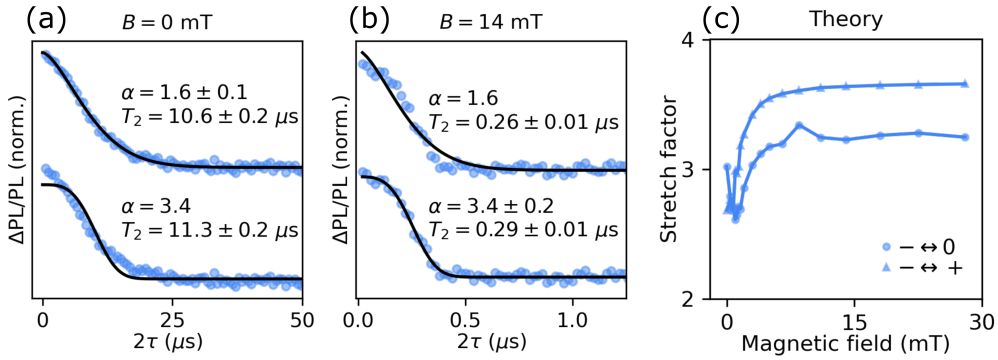

FIG. S7. Magnetic-field dependent stretch factors for **2**. (a), (b), a fit to the stretch factor α at zero magnetic field yields a different value than at higher fields. Choosing either the zero-field or 14 mT α for both fields results in deviations from the observed traces. However, the extracted T_2 times do not depend strongly on the choice of α. (c) Stretch factors for **2** calculated through gCCE.

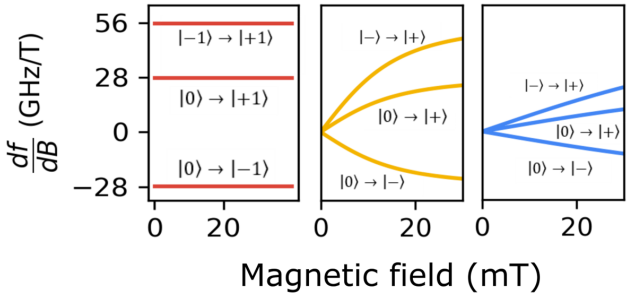

FIG. S8. df/dB for **1**, **3,** and **2**.

we effectively have a two-level system, since the $|-\rangle \leftrightarrow |+\rangle$ transition is forbidden, and microwave pulses generate coherences between only two levels (similarly for z-polarised microwaves). For an arbitrary microwave polarisation however, coherences can be generated across all three spin sublevels. To understand the role of this in our experiments we performed numerical simulations of a Hahn-echo sequence for a microwave drive $\propto (S_y + S_z)$, such that both transitions can be driven simultaneously. We performed these calculations with $E = D/3$ (degenerate transitions) and compared them to the non-degenerate case $E = D/3 - \Delta$, where Δ is an offset to break the transition degeneracy. We found the T_2 was essentially unchanged between these cases (and robust to pulse errors and imperfect optical initialization and readout fidelities) indicating that the transition degeneracy does not play a major role in the extracted zero-field T_2 for **2**.

T_2 for 4. As a fourth system to examine the dependence of T_2 on transverse zero-field splitting, we also measured T_2 at zero field for **4**, i.e., Cr(IV)(2,4-dimethylphenyl)$_4$ diluted in Sn(2,4-dimethylphenyl)$_4$ [Fig. S9(a)] which has a similar $E \simeq 0.5$ GHz to **3** [3]. We find a similar T_2 to **3** consistent with the similar E values of **3** and **4**.

ODMR linewidths and $T_2^\star$. For **1**, **2**, and **3** we observe full-width half-maximum ODMR linewidths of $\Delta f \simeq$40, 40, and 110 MHz respectively. Extracting an inhomogeneous spin coherence time $T_2^\star$ from these linewidths using $T_2^\star = 1/(\pi \Delta f)$ yields $T_2^\star = 3 - 8$ ns. These linewidths therefore currently make it challenging to perform Ramsey experiments although this would be a valuable experiment for future work on lower-linewidth samples. We note that the ensemble ODMR linewidths have contributions from strain inhomogeneities–which result in shifts in the zero-field splitting–as well as the surrounding nuclear spins, and therefore do not necessarily correlate with the variation in the E-parameter.

Other decoherence sources. Due to the high nuclear-spin density in these molecular systems, we expect the nuclear spin bath to constitute the main source of decoherence through magnetic-field noise. Cr^{4+} electron spins provide an additional source of magnetic-field noise. A first-order sensitivity to electric fields can further contribute to decoherence at clock transitions [11], however, since these molecular systems are electrically neutral, we do not expect a major contribution from charge noise, in contrast to color centers in semiconductors. Other possible decoherence

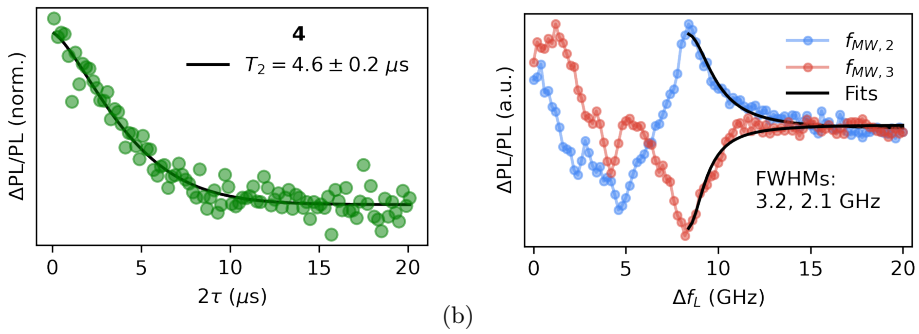

FIG. S9. (a) Zero-field Hahn echo for **4**, with stretch factor $\alpha = 1.4 \pm 0.1$. (b) ODMR as a function of laser sideband frequency Δf_L. Fits are to the response around the high-frequency spin transition at $\simeq 8.3$ GHz only to reduce the effect of multiple overlapping resonances.

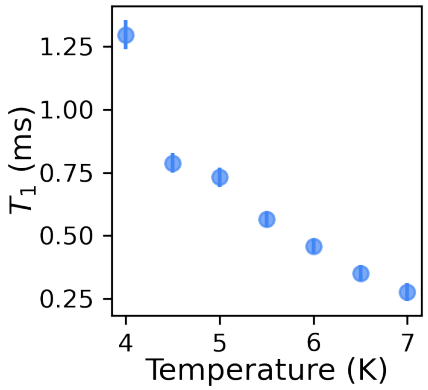

FIG. S10. T_1 for **2** as a function of temperature.

contributions can arise from strain modulation of the zero-field splitting. However, since the gCCE calculations—which only consider magnetic field noise from the nuclear spin bath—agree with the experimental measurements, other decoherence sources appear to play a less important role.

Homogeneous linewidth extraction. In Fig. 4(d) of the main text, to extract the homogeneous linewidth of **2** we perform ODMR as a function of Δf_L, the frequency applied to a (phase) electro-optic modulator (EOM). In these experiments, we expect a decrease in ODMR contrast (relative to large detunings of Δf_L) when Δf_L is equal to the ODMR drive frequency, $f_{\mathrm{MW},i}$. Similarly, we expect an increase in ODMR contrast when $\Delta f_L = 0$ and when Δf_L is equal to the frequencies of the undriven spin transitions, $f_{\mathrm{MW},j\neq i}$ (determined from the ODMR spectrum). Applying $f_{\mathrm{MW},2}$ we therefore expect a dip in contrast around $\Delta f_L = f_{\mathrm{MW},2}$, and peaks around $\Delta f_L = 0, f_{\mathrm{MW},1}, f_{\mathrm{MW},3}$. Similarly, applying $f_{\mathrm{MW},3}$, we expect a dip in contrast around $\Delta f_L = f_{\mathrm{MW},3}$, and peaks around $\Delta f_L = 0, f_{\mathrm{MW},1}, f_{\mathrm{MW},2}$. Applying Δf_L to our EOM generates sidebands at $f_L \pm \Delta f_L$ but also generates unwanted higher harmonics, e.g., second harmonics at $f_L \pm 2\Delta f_L$. These harmonics will therefore also contribute to the observed traces. To fit the experimental traces, taking into account the second-harmonic response, we use a function consisting of Lorentzian dips at $\Delta f_L = f_{\mathrm{MW},i}, \frac{1}{2} f_{\mathrm{MW},i}$ and Lorentzian peaks at $\Delta f_L = 0, \{f_{\mathrm{MW},j\neq i}\}, \frac{1}{2}\{f_{\mathrm{MW},j\neq i}\}$. A single linewidth is used for all of the Lorentzian components, whose magnitudes are used as free parameters. The fits in the main text carried out with this procedure yielded a linewidth (full-width half maximum) of 3.1 GHz for the $f_{\mathrm{MW},2}$ trace and 2.5 GHz $f_{\mathrm{MW},3}$ trace. As an alternative method to extracting the homogeneous linewidth from these traces, we fit a single Lorentzian to the peak (or dip) around $\Delta f_L = f_{\mathrm{MW},3}$ only [Fig. S9(b)]. In this region, higher laser harmonics will not be resonant with any spin transitions, so the response can be fit with a single Lorentzian. Fig. S9(b) shows the corresponding fits using this approach where we fit only the higher-frequency side of the response to reduce the effect of any overlapping transitions. We find linewidths of 3.2 GHz for the $f_{\mathrm{MW},2}$ trace and 2.1 GHz $f_{\mathrm{MW},3}$ trace, similar to the approach used in the main text in which the response for all Δf_L values is fit.

Temperature dependence of T_1. Fig. S10 shows the temperature dependence of the spin-lattice relaxation time for **2** measured using the all-optical sequence outlined in the main text. We find that T_1 decreases roughly fourfold as the temperature is lowered from 4 K to 7 K, indicating that the improved T_1 in **2** compared to **1** could arise from

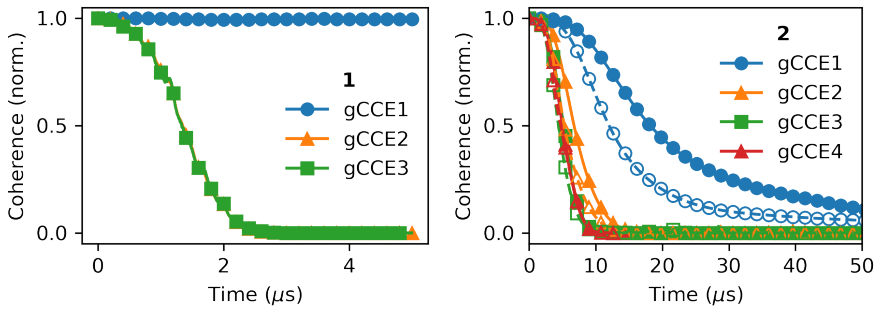

FIG. S11. Simulated Hahn echo traces at zero magnetic field for **1** and **2** as a function of gCCE order. For **2**, filled makers are the $|0\rangle \leftrightarrow |-\rangle$ transition, while unfilled markers are the $|-\rangle \leftrightarrow |+\rangle$ transition.

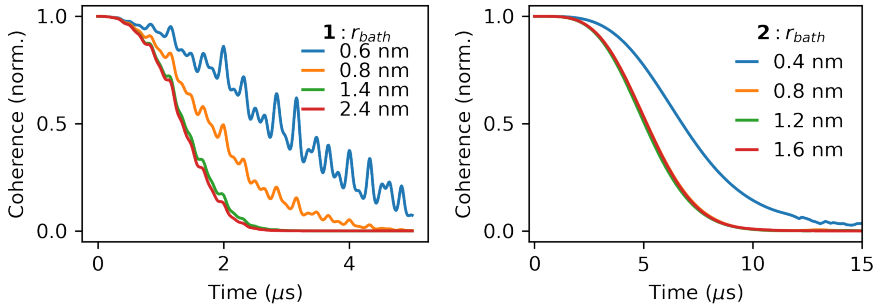

FIG. S12. Simulated Hahn echo traces at zero magnetic field for **1** and **2** ($|0\rangle \leftrightarrow |-\rangle$ transition) as a function of the bath radius r_{bath}.

a lower local temperature through improved thermalization.

V. CLUSTER CORRELATION EXPANSION (CCE) CALCULATIONS

Computational details. CCE simulations were performed using the PyCCE library [12], and to accurately model clock transitions, we used the generalized CCE (gCCE) formulation, described in detail in Ref. [12]. The hyperfine couplings within the Cr-containing molecule and the Cr spin density distribution were computed using density functional theory (DFT) with the SCAN functional and a def2-TZVP gaussian basis set using the ORCA package [13]. Using the calculated Cr spin density distribution, the hyperfine couplings between the Cr spin and the surrounding matrix nuclear spins A_{ij} were calculated using the dipole approximation as

$$A_{ij} = \frac{1}{2S}\frac{\mu_0}{4\pi}\gamma_e\gamma_n \int \frac{(\mathbf{r}-\mathbf{r}_n)^2\delta_{ij} - 3(\mathbf{r}-\mathbf{r}_n)_i(\mathbf{r}-\mathbf{r}_n)_j}{|\mathbf{r}-\mathbf{r}_n|^3} n_s(\mathbf{r})d\mathbf{r}$$

where i, j are cartesian components (x, y, z), $S = 1$ is the electron spin multiplicity, γ_e, γ_n are the gyromagnetic ratios of the electronic and nuclear spins, $\mathbf{r}_n$ is the nuclear spin position, and $n_s(\mathbf{r})$ is the electronic spin density at position $\mathbf{r}$. We used point dipole-dipole interactions between nuclear spins.

gCCE order convergence. Fig. S11 shows the calculated Hahn echo traces for **1** and **2** with increasing gCCE order, where gCCEn indicates inclusion of clusters containing up to n nuclei. For **1** we find convergence for gCCE2, i.e., including the contribution of clusters of up to two nuclei, while for **2** we find convergence for gCCE3, i.e., including the contribution of clusters of up to three nuclei. We therefore use gCCE3 for predicting the spin dynamics for **2**.

Bath size. Fig. S12 shows the calculated Hahn echo traces for **1** and **2** as a function of the bath radius r_{bath}, showing convergence by $r_{\mathrm{bath}} \simeq 1.5\,\mathrm{nm}$. In the main text we use $r_{\mathrm{bath}} = 1.5 - 2\,\mathrm{nm}$.

Connectivity radius. Fig. S13 shows the calculated Hahn echo traces for **1** and **2** as a function of the connectivity radius - the maximum distance between two bath spins to be considered in the same cluster. We used a value of $r_{\mathrm{dipole}} = 0.6\,\mathrm{nm}$. This value corresponds to about 1,700 nuclear spins and 32,000 nuclear spin pairs at $r_{\mathrm{bath}} = 2\,\mathrm{nm}$. The number of higher order clusters was cut off at 5×10^5 clusters.

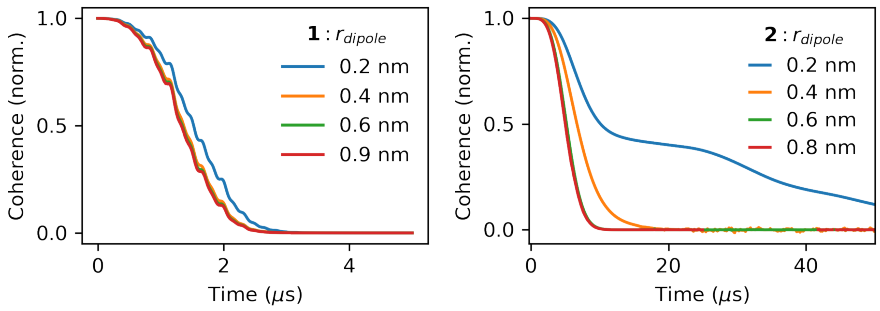

FIG. S13. Simulated Hahn echo traces at zero magnetic field for **1** and **2** ($|0\rangle \leftrightarrow |-\rangle$ transition) as a function of the connectivity radius, r_{dipole}.

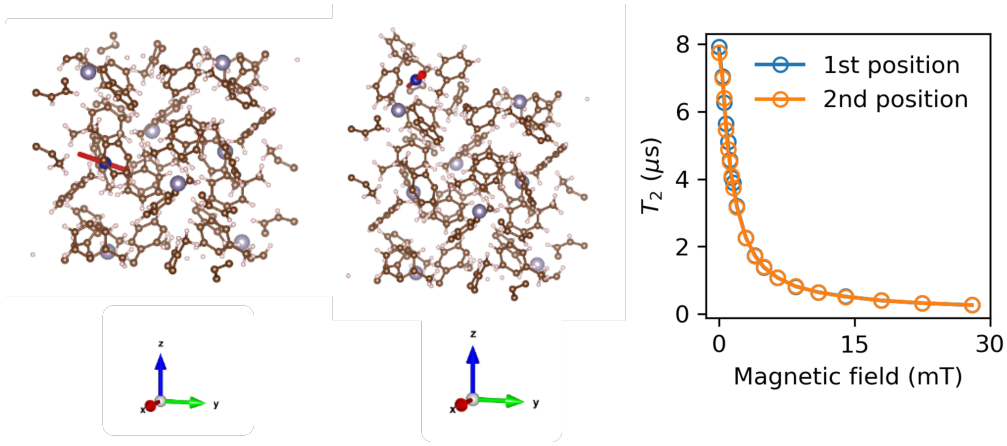

FIG. S14. Simulated T_2 times for **2** ($|0\rangle \leftrightarrow |-\rangle$ transition) as a function of magnetic field for two different configurations of the Cr molecule (red arrow) in the **2-Sn** unit cell. The direction of the red arrow of the Cr site represents the assumed quantization axis of the Cr molecule.

Cr-site dependence in 2. Since there are mutliple sites within the unit cell of **2-Sn**, we simulated the coherence from two different sites from the crystal structure of **2-Sn** (Fig. S14). The gCCE calculations show little dependence of the coherence time on the molecule's orientation indicating preceise site assignment was not key.

Coherence function under an applied magnetic field. In the calculated coherence function of the $|0\rangle \leftrightarrow |-\rangle$ transition of **2** under an applied magnetic field, revivals of the Hahn-echo signal start to appear. To be consistent with the experimental data, the fitting of T_2 from the simulated Hahn-echo traces was performed only before the revivals.

Magnetic-field orientation dependence. Fig. S15 shows the dependence of the calculated coherence times

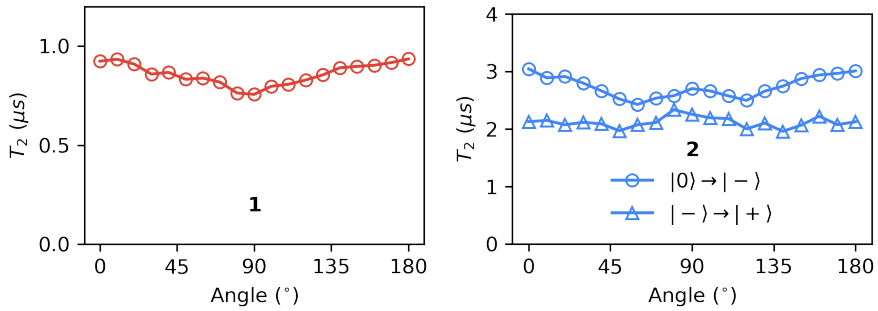

FIG. S15. Simulated T_2 times for **1** and **2** as a function of the angle between a 2 mT magnetic field and the z-axis of the Cr zero-field splitting tensor, showing a weak orientation dependence.

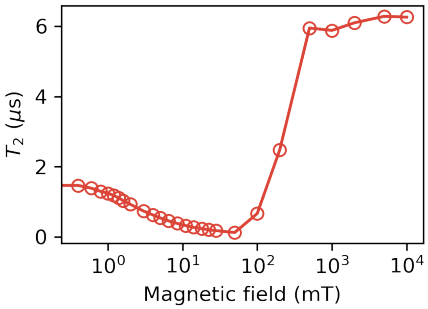

FIG. S16. Simulated T_2 times vs magnetic field for **1** up to 10 T.

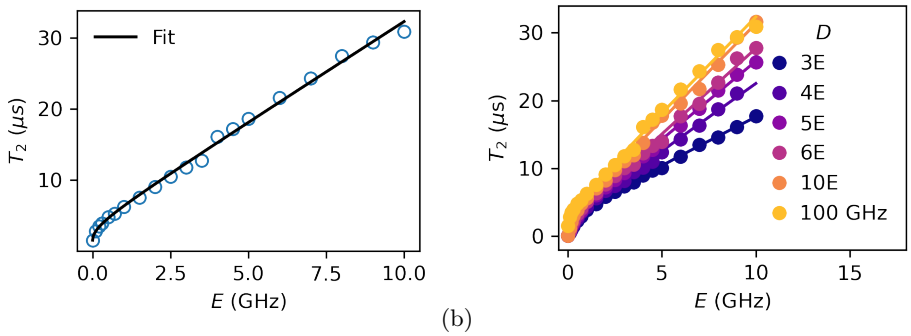

(a) (b)

FIG. S17. (a) Simulated T_2 times vs transverse zero-field splitting E along with a fit to the functional form $T_2 = a\sqrt{(E+b)^2 - b^2)} + c$, used as the trace in Fig. 3(c), where $a = 2.8\,\mu$s/GHz, $b = 0.96\,$GHz, $c = 1.5\,\mu$s. (b) Simulated T_2 times vs transverse zero-field splitting E for different D parameters, along with fits to the above functional form.

as a function of the magnetic-field orientation. The weak dependence observed here is also observed experimentally (Fig. S5) and indicates that our results are not sensitive to precise magnetic-field alignment.

High-field recovery of T_2. Fig. S16 shows calculated coherence times up to high (10 T) magnetic fields for **1**, showing the high-field recovery of the coherence. We were not able to reach sufficiently high fields in our optical experiments to observe this recovery but note that inductively detected electron spin resonance experiments performed at $\simeq 400\,$mT on **1** gave $T_2 \simeq 2.5\,\mu$s [14], consistent with the simulated behavior.

T_2 vs E. Fig. S17(a) shows the simulated T_2 vs E parameter. To consider only the role of E, and not D, we take $D = 100\,$GHz for concreteness but note that there is some dependence on the D-parameter - Fig. S17(b).The first-order noise sensitivity df/dB (Fig. S8) depends only on E, and so to a first approximation the magnitude of D may not be expected to be relevant in determining T_2. However, a dependence of T_2 on D [Fig.S17(b)] likely arises from higher-order hyperfine-mediated intrabath interactions, which depend on the energetic separation of all levels (see Ref. [15]). We note that the value of D sets the upper bound for E and hence is important for being able to realise a given E parameter, and, in addition, is also important in determining the fidelity of spin-selective excitation.

[1] S. U. Koschmieder, B. S. McGilligan, G. McDermott, J. Arnold, G. Wilkinson, B. Hussain-Bates, and M. B. Hursthouse, Aryl and aryne complexes of chromium, molybdenum, and tungsten. x-ray crystal structures of [cr (2-mec6h4)(μ-2-mec6h4)(pme3)] 2, mo (η2-2-mec6h3)(2-mec6h4) 2 (pme2ph) 2, and w (η2-2, 5-me2c6h2)(2, 5-me2c6h3) 2-(pme3) 2, J. Chem. Soc., Dalton Trans. , 3427 (1990).
[2] C. Schneider-Koglin, B. Mathiasch, and M. Dräger, Über tetraaryl-methan-analoga in der gruppe 14: Iii. ar4sn/pb (ar ph, p-, m-, o-tol, 2, 4-xyl und 2, 5-xyl): Gegenüberstellung von bindungslängen und winkeln, von nmr chemischen verschiebungen und kopplungskonstanten und von schwingungsdaten, J. Organomet. Chem. **469**, 25 (1994).
[3] S. Bayliss, D. Laorenza, P. Mintun, B. Kovos, D. E. Freedman, and D. Awschalom, Optically addressable molecular spins for quantum information processing, Science **370**, 1309 (2020).
[4] Rigaku, *CrysAlisPro Software System, Version 1.171. 38.41 l, Rigaku Coorporation* (Rigaku Oxford Diffraction, UK, 2015).
[5] O. V. Dolomanov, L. J. Bourhis, R. J. Gildea, J. A. K. Howard, and H. Puschmann, Olex2: A complete structure solution, refinement and analysis program, J. Appl. Cryst. **42**, 339 (2009).

[6] G. M. Sheldrick, *SHELXT* – integrated space-group and crystal-structure determination, Acta Cryst. A **71**, 3 (2015).
[7] G. M. Sheldrick, Crystal structure refinement with *shelxl*, Acta Cryst. C **71**, 3 (2015).
[8] J. F. Barry, J. M. Schloss, E. Bauch, M. J. Turner, C. A. Hart, L. M. Pham, and R. L. Walsworth, Sensitivity optimization for nv-diamond magnetometry, Reviews of Modern Physics **92**, 015004 (2020).
[9] Ł. Cywiński, Dynamical-decoupling noise spectroscopy at an optimal working point of a qubit, Physical Review A **90**, 042307 (2014).
[10] N. Zhao, S.-W. Ho, and R.-B. Liu, Decoherence and dynamical decoupling control of nitrogen vacancy center electron spins in nuclear spin baths, Physical Review B **85**, 115303 (2012).
[11] P. Jamonneau, M. Lesik, J. Tetienne, I. Alvizu, L. Mayer, A. Dréau, S. Kosen, J.-F. Roch, S. Pezzagna, J. Meijer, *et al.*, Competition between electric field and magnetic field noise in the decoherence of a single spin in diamond, Physical Review B **93**, 024305 (2016).
[12] M. Onizhuk and G. Galli, Pycce: A python package for cluster correlation expansion simulations of spin qubit dynamics, Advanced Theory and Simulations **4**, 2100254 (2021).
[13] F. Neese, The orca program system, Wiley Interdisciplinary Reviews: Computational Molecular Science **2**, 73 (2012).
[14] D. W. Laorenza, A. Kairalapova, S. L. Bayliss, T. Goldzak, S. M. Greene, L. R. Weiss, P. Deb, P. J. Mintun, K. A. Collins, D. D. Awschalom, *et al.*, Tunable cr4+ molecular color centers, Journal of the American Chemical Society **143**, 21350 (2021).
[15] W. Yao, R.-B. Liu, and L. Sham, Theory of electron spin decoherence by interacting nuclear spins in a quantum dot, Physical Review B **74**, 195301 (2006).